Journal of Sound and Vibration (1999) **222**(3), 363–388
Article No. jsvi.1998.1990, available online at http://www.idealibrary.com on IDEAL

ACTIVE CONTROL OF SOUND RADIATION FROM CYLINDERS WITH PIEZOELECTRIC ACTUATORS AND STRUCTURAL ACOUSTIC SENSING

J. P. MAILLARD AND C. R. FULLER

Vibration and Acoustics Laboratories,
Virginia Polytechnic Institute and State University, *Blacksburg*, *VA* 24061-0238,
U.S.A.

(*Received* 7 *November* 1997, *and in final form* 23 *September* 1998)

In this paper, analytical and experimental results of an investigation of active control of sound radiated from cylinders are presented. The aluminium cylinder is 1 m in length, 25 cm in diameter and 2·4 mm in thickness with two rigid end-caps at both ends. The excitation is a band-limited random noise encompassing the first five modes of the cylinder and the control actuators are surface mounted piezoelectric transducers. Since it is desired to integrate the error sensors into the structure, the recently developed Discrete Structural Acoustic Sensing (DSAS) approach is extended to the cylindrical co-ordinates and implemented using 12 accelerometers mounted on the cylinder. The structural acoustic sensor provides times domain estimates of far-field radiated sound at predetermined radiation angles. The controller is a 3 by 3 Filtered-x LMS paradigm implemented on a TMS320C30 DSP. The results show good global control of the radiated sound over the frequency bandwidth of excitation. Most important, the proposed discrete structural acoustic sensor yields similar performances as error microphones located in the far field. The sensor is also shown to improve far-field attenuation over minimization of normal acceleration at discrete locations on the cylinder structure.

1. INTRODUCTION

Much research has been conducted in the active control of low-frequency structure-borne sound. When compared to passive methods, active control presents significant advantages in the low-frequency range where passive control becomes often impractical due to prohibitive volume and/or mass requirements. For the past decade, Active Structural Acoustic Control (ASAC) has received much attention as it presents a practical alternative to the control of low-frequency structurally radiated noise [1, 2]. In this technique, the radiated sound pressure is attenuated by applying mechanical inputs directly to the structure rather than by exciting the surrounding medium with acoustic sources (Active Noise Control).

0022–460X/99/180363 + 25 $30.00/0

Piezoelectric devices have been applied extensively to Active Structural Acoustic Control systems as structural actuators [3–5] thus yielding a compact or "smart" structure. In an attempt to further reduce the size of the overall control arrangement, the microphones traditionally located in the far field to provide radiation error information are also being replaced by structural sensors such that all transducers are integrated in the structure.

As most ASAC applications involve noise control below the coincidence frequency of the radiating structure, appropriate structural sensors for ASAC should only observe the radiating part of the structural vibrations. This gives more flexibility to the controller which in some situations modifies the structural vibrations such as to attenuate far-field radiation with no net reduction in the overall vibration levels. Sound attenuation in the far field can then be achieved with a reduced control authority compared to cases where all structural motion is cancelled (Active Vibration Control) [6].

With the emergence of polyvinylidene fluoride (PVDF) as a sensor material, several structural sensors for ASAC have been proposed to observe the radiating part of the structural vibrations. Most of these sensing techniques are based on modal sensing [7]: the sensor effectively observes a specific set of modes of vibration (natural or radiation modes of the uncontrolled response) which couples well to far-field radiation [8–11]. An accurate knowledge of the structure's dynamic properties is therefore required. Recently, an alternative sensing technique referred to as Discrete Structural Acoustic Sensing (DSAS) was demonstrated both analytically [12, 13] and experimentally [14, 15] on baffled planar radiators. The technique implements an array of structural point sensors whose outputs are passed through digital FIR filters to estimate in real time the far-field radiated pressure in a given direction, or equivalently, a given wave-number component, over a broad frequency range. It uses the relation between the structural out-of-plane vibrations and the far-field sound pressure as defined by the Helmholtz integral. One of the significant advantages of this strategy lies in its low modelling requirements compared to modal sensing approaches. In particular, the sensor design does not require the knowledge of the structural mode shapes and thus remains largely independent of the boundary conditions. Consequently, it is particularly well adapted for feedforward control approaches commonly used in ASAC systems where no analytical system modelling is necessary. It also provides time domain information which is required by the Filtered-x LMS algorithm commonly used in feedforward control. This paper presents analytical and experimental results on the extension of Discrete Structural Acoustic Sensing to baffled cylindrical radiators.

Most of the work on ASAC systems deals with planar geometries or systems than can be decomposed in a set of planar radiators and few reports of experiments on cylindrical structures can be found in the literature. Ruckman and Fuller [16] reported numerical simulations of ASAC applied to a finite cylinder system. Previous work by Clark and Fuller [17] studied experimentally the harmonic control of sound radiation from a finite enclosed cylinder using PVDF error sensors and piezoelectric actuators. Results showed the PVDF sensor was effective in observing the longitudinal extensional waves of the cylinder ("accordion"

modes) and thus, good sound attenuation was obtained for this type of excitation. However, very little attenuation was achieved for radial excitations (normal bending modes) due to the relatively high modal density of the cylinder. The present study extends the above work by considering broadband radiation control over the first five bending modes of the structure. After briefly introducing the theoretical formulation, analytical and experimental results are presented. In both cases, the discrete structural acoustic sensor is first studied in terms of its accuracy to predict radiated pressure. Broadband radiation control results are then discussed by comparing the performances of the sensor to those of error microphones located in the far field.

2. THEORETICAL BASIS

This section presents the analytical formulation of Discrete Structural Acoustic Sensing. A relation between discrete structural acceleration and the far-field pressure estimate is derived for the case of baffled cylindrical geometries.

2.1. FAR-FIELD SOUND PRESSURE

For the general case of arbitrary geometries, the sound pressure radiated from a vibrating structure into an unbounded medium can be expressed using the Kirchhoff–Helmholtz integral formulation [18]. Assuming a harmonic solution for the pressure, $p(\mathbf{r})\,e^{j\omega t}$, where ω is the angular frequency, this is expressed as

$$p(\mathbf{r}) = \int_{S_0}\int \left[\rho G(\mathbf{r}|\mathbf{r}_0)\ddot{w}(\mathbf{r}_0) + p(\mathbf{r}_0)\frac{\partial G}{\partial \eta_0}(\mathbf{r}|\mathbf{r}_0) \right] \mathrm{d}S(\mathbf{r}_0), \quad \mathbf{r}\in V. \tag{1}$$

In the above equation, S_0 denotes the radiating surface and V the surrounding volume. The sound pressure $p(\mathbf{r})$ at field point $\mathbf{r}$ is expressed as a surface integral involving the out-of-plane structural acceleration, $\ddot{w}(\mathbf{r}_0)$, measured at location $\mathbf{r}_0$ on the radiating surface, the surface pressure $p(\mathbf{r}_0)$, the Green's function, $G(\mathbf{r}|\mathbf{r}_0)$, and its normal gradient ($\partial G/\partial \eta_0$ represents the component of the gradient of G along the unit vector $\boldsymbol{\eta}$ normal to S_0), and the fluid density, ρ. Note that this formulation assumes the radiator has solid boundaries such that the fluid velocity on the boundary is equal to the structural out-of-plane velocity. The normal pressure gradient then becomes equal to $\rho\ddot{w}(\mathbf{r}_0)$. Discrete Structural Acoustic Sensing is based on the existence of a Green's function satisfying the Neumann boundary condition,

$$\frac{\partial G}{\partial \eta_0}(\mathbf{r}|\mathbf{r}_0) = 0, \quad \mathbf{r}\in S_0, \tag{2}$$

such that the radiated pressure field becomes solely dependent on the structural acceleration and geometry.

For baffled cylindrical geometries (see Figure 1), a closed-form solution exists for the Green's function verifying equation (2). The radiated pressure is then expressed in the cylindrical co-ordinate system (R, θ, ϕ) as

$$p(R, \theta, \phi) = \rho \int_0^{2\pi} \int_{-L}^{+L} G(R, \theta, \phi | r = a, \phi', z') \ddot{w}(\phi', z') a \, \mathrm{d}\phi' \, \mathrm{d}z'. \tag{3}$$

The Green's function in equation (3) can be obtained from the radiated pressure due to a point acceleration distribution located on an infinite cylindrical baffle. The resulting expression is approximated in the far field as [18]

$$G(R, \theta, \phi | a, \phi_o, z_0) = -\frac{\exp[-jk(R - z_0 \cos\theta)]}{\pi^2 akR \sin\theta} \sum_{n=0}^{+\infty} \frac{j^{n+1}}{\varepsilon_n} \frac{\cos[n(\phi - \phi_0)]}{H_n^{(2)'}(ka \sin\theta)}, \tag{4}$$

where $\varepsilon_n = 2$ for $n = 0$ and $\varepsilon_n = 1$ for $n > 0$ (n integer). The function $H_n^{(2)'}(x)$ denotes the first derivative of the nth Hankel function of the second kind [19]. Here n represents the circumferential modal order. The acoustic wave-number is denoted as $k = \omega/c$ where c is the speed of sound. The various co-ordinates and dimensions involved in equation (4) are shown in Figure 1.

2.2. SENSOR ESTIMATE

An estimate of the radiated pressure in equation (3) is now constructed. The integral over the radiating surface S_0 is approximated using a Q point zero-order interpolation of the acceleration distribution [15], i.e., the acceleration is assumed

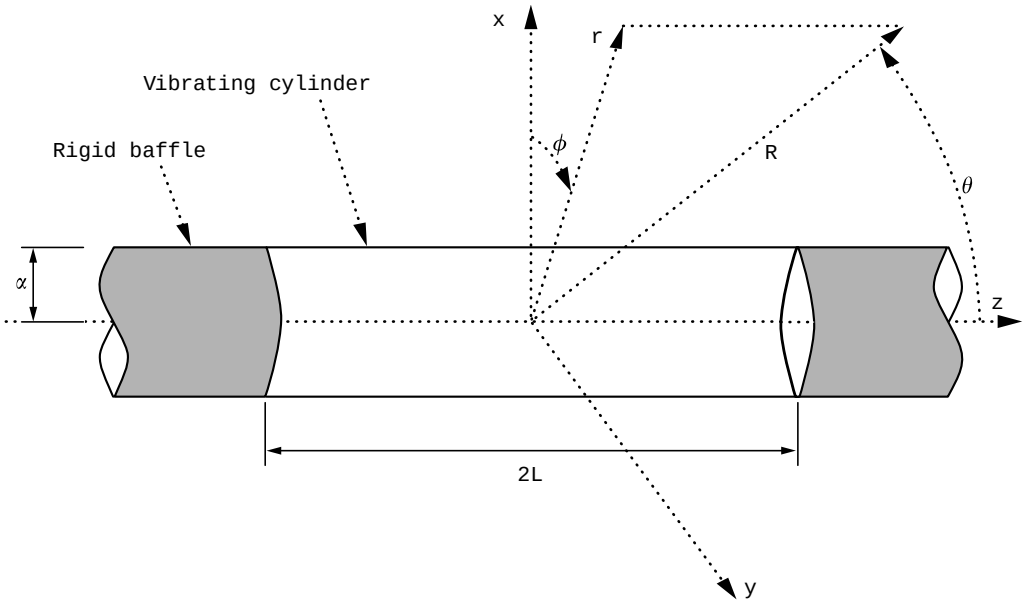

Figure 1. Baffled cylindrical geometries.

constant over Q small elemental surfaces, S_q, $q = 1, 2 \ldots, Q$, such that $S = \cup_{q=1}^{Q} S_q$. The resulting pressure estimate takes the general form

$$p_d(R, \theta, \phi, t) = \sum_{q=1}^{Q} \ddot{w}(\phi_q, z_q, t) H_q(R, \theta, \phi), \tag{5}$$

where (ϕ_q, z_q) represents the co-ordinates of the qth node, and $H_q(R, \theta, \phi)$, the associated sensor transfer function. Defining $S_q = a\Delta z_q \Delta\phi_q$ as the qth elemental surface aligned with the axial and circumferential directions such that its center coincides with (ϕ_q, z_q), the sensor transfer functions can be expressed as

$$H_q(R, \theta, \phi) = \rho \int_{z_q - \Delta z_q/2}^{z_q + \Delta z_q/2} \int_{\phi_q - \Delta\phi_q/2}^{\phi_q + \Delta\phi_q/2} G(R, \theta, \phi | a, \phi', z') a \, \mathrm{d}\phi' \, \mathrm{d}z'. \tag{6}$$

The transfer function $H_q(R, \theta, \phi)$ can be interpreted physically as the sound pressure radiated at (R, θ, ϕ) from the qth elemental surface vibrating along the normal to its center (ϕ_q, z_q) with a unit acceleration. In other words, the pressure estimate is constructed by summing the radiation contribution of Q cylindrical pistons weighted by the measured acceleration amplitudes. It is thus referred to as the piston approximation. Assuming the Green's function remains almost constant over each surface S_q, the transfer function in equation (6) can be replaced by $\rho a \Delta z_q \Delta\phi_q G(R, \theta, \phi | a, \phi_q, z_q)$. In this case, the far-field pressure is estimated from the contribution of Q monopole sources (monopole approximation). As expected, both approximations become equivalent as $k \max(\Delta z_q, \Delta\phi_q) \ll 1$.

It should be stressed that the sensor transfer functions solely depend on the geometry of the problem and the properties of the fluid medium. No accurate knowledge of the structure's dynamics (e.g., natural mode shapes) is thus required for their design. Note however that some information is still needed in order to determine an appropriate discretization level for accurate estimates. Furthermore, the sensing approach can be extended to geometries for which no Green's function is available analytically. The far-field pressure radiated from each elemental surface vibrating independently on the structure's boundary must then be solved numerically using a technique such as the Boundary Element Method [20].

3. PRACTICAL IMPLEMENTATION

This section briefly recalls some of the important issues associated with the practical implementation of Discrete Structural Acoustic Sensing. The pressure estimate presented in the previous section is implemented on a real system using a set of accelerometers mounted on the structure and arrays of digital filters. More precisely, each measured acceleration signal is pased through a digital filter modelling the associated sensor transfer function. All filter outputs are then summed to provide the sound pressure estimate. Several arrays of filters can be implemented in order to provide pressure estimates at different locations. This arrangement is shown in Figure 2 along with a schematic of the controller based on the three channel Filtered-x LMS algorithm.

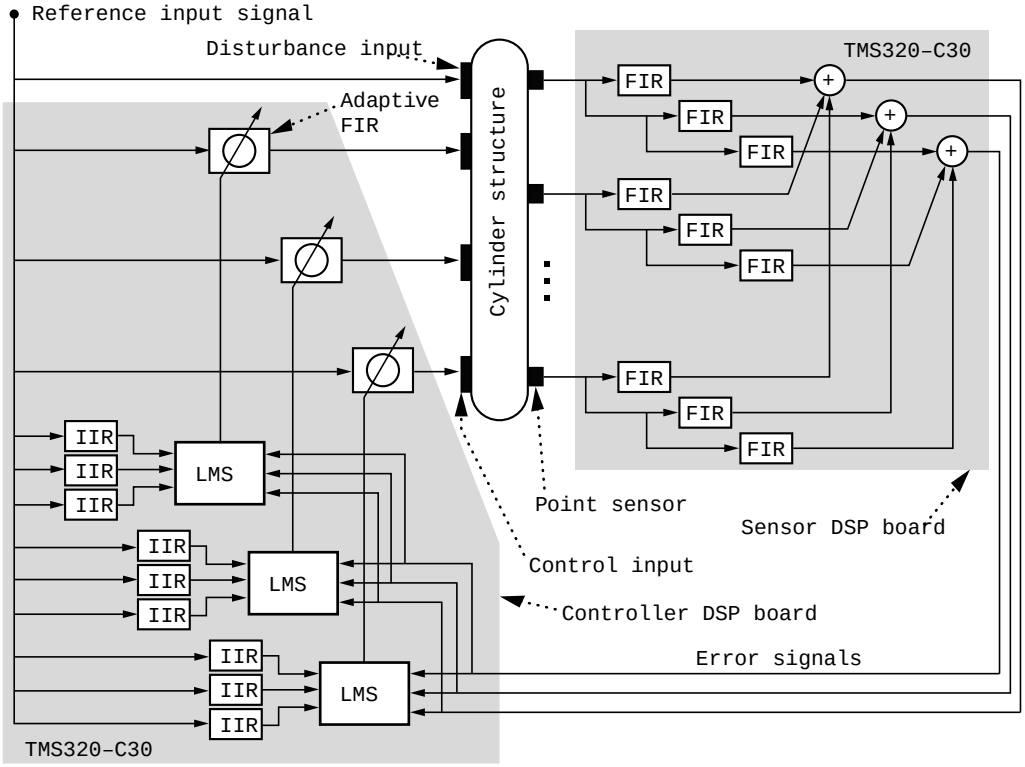

Figure 2. Schematic of the discrete structural acoustic sensor along with the three-channel feedforward controller.

As explained above, each transfer function represents the far-field radiation into an unbounded medium from a cylindrical piston source (or monopole) with unit acceleration and located on a cylindrical baffle. The associated characteristics directly motivate the use of Finite Impulse Response (FIR) filters to model the sensor transfer functions. In particular, no resonance behavior occurs due to the assumption of an unbounded medium at infinity and notches in the transfer functions magnitude associated with zero pressure angles are easily modelled by appropriate zeros in the filter's impulse response.

Another important issue is related to the time delay of the sensor transfer functions, which is directly related to the acoustic path propagation time, R/c. As the pressure estimate is only valid in the far field, this delay can become significant compared to the sampling period of the digital filter, thus increasing its complexity. The authors have shown in previous work, however, that error signals based on far-field pressure at a given location can be shifted in time without loss of performance of the control system (the time shift is equivalent to moving the minimization point along a constant radiation angle) [15]. Removing the above time delay yields transfer functions with a minimum phase delay which significantly reduces the number of FIR filter coefficients required for accurate modelling.

4. SYSTEM CHARACTERISTICS AND EXPERIMENTAL SET-UP

Testing of the structural acoustic sensor described above was performed on a finite aluminum cylinder. This section presents the main characteristics of the system, the control and measurement set-ups implemented in the experiments, as well as the numerical model of the structure.

4.1. SYSTEM CHARACTERISTICS

Due to a limited number of accelerometers available for implementing Discrete Structural Acoustic Sensing, the choice of the cylinder's dimensions and material was made such that the first few flexural modes of the structure have low modal order in both the axial and circumferential directions. The cylinder characteristics are given in Table 1. The dimensions were measured on the actual structure while the material properties are based on standard values for aluminum. In order to allow structural vibration measurements over the entire surface of the cylinder as well as acoustic measurements over the sphere surrounding the structure, the cylinder's attachment to its support stand is designed to allow full rotation along its main axis. The cylinder is closed at both ends by aluminum end-caps 12·7 mm in thickness. Each end-cap is attached to the cylinder with a set of 12 small screws equally spaced along the circumference. A steel rod 3·18 mm in diameter is threaded into each end-cap and mounted on a nylon ring. The ring is fixed in a 19·1-mm aluminum section which is bolted to a heavy steel support stand. To allow acoustic measurements of the baffled structure, two sections of "rigid" PVC pipe are installed on each side of the cylinder along its main axis. The two pipes extend in length up to the walls of the anechoic chamber. A picture of the complete rig including the baffle is shown in Figure 3.

All structural vibration inputs, i.e., both disturbance and control inputs, are applied through single-sided piezoelectric actuators. No curved actuators were available for the experimental testing and flat actuators [21] were mounted on the cylinder by cutting them across their width into a set of eight strips of same dimensions. The original actuators are 63·5 mm in length and 38·1 mm in width, which results in eight 7·9 by 38·1 mm strips. They are mounted on the cylinder's

TABLE 1

Dimensions and material properties of the cylinder and piezoelectric actuators

Parameter	Cylinder	Actuators
Length (mm)	987	38·1
Outside diameter/width (mm)	254	69·9
Thickness, (mm)	2·36	0·1905
Young's modulus (N/m^2)	$7{\cdot}1 \times 10^7$	$6{\cdot}1 \times 10^{10}$
Poisson ratio	0·31	0·33
Mass density (kg/m^3)	2700	7750
d_{31} constant (m/V)	–	171×10^{-12}
Hysteretic damping factor	0·002	0

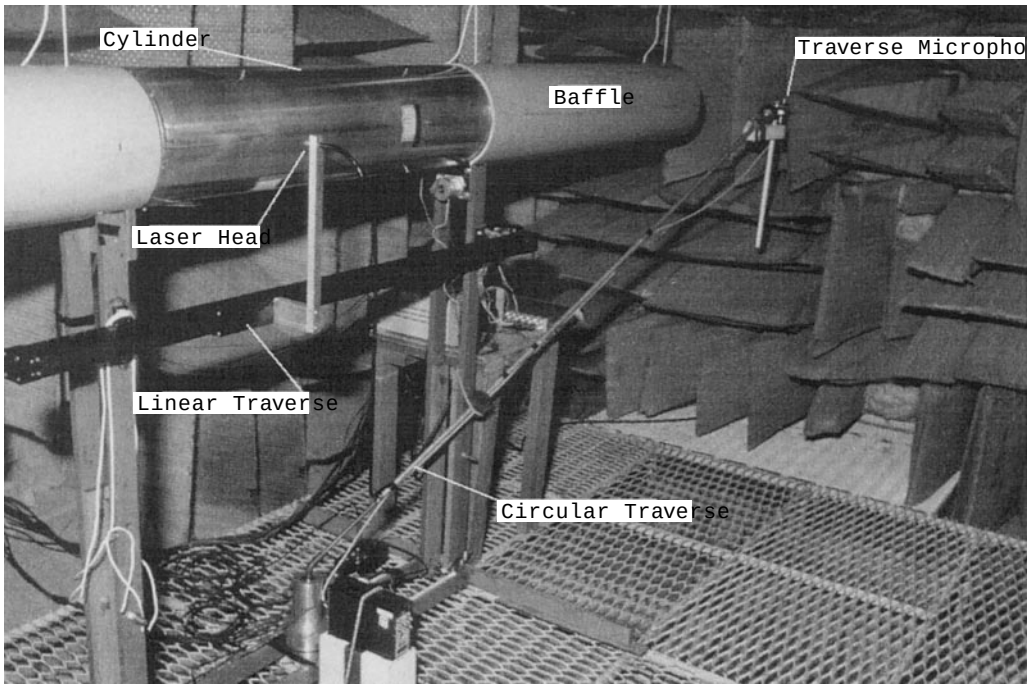

Figure 3. Cylinder rig inside the anechoic chamber.

outside surface side by side with their length along the cylinder's axis and wired in phase. A gap of approximately 1 mm remains between each actuator strip to avoid short circuits between the electrodes of two adjacent actuators. The total surface area covered by the set of eight actuators is 69·9 by 38·1 mm. Table 1 presents the dimensions and material properties of the piezoelectric actuators. Four sets of the actuator arrangement described above are mounted on the cylinder according to the center locations given in Table 2. The disturbance actuator center location serves as the origin of the circumferential direction, $\phi = 0^\circ$. Its axial location, $z/L = -0{\cdot}328$, ensures that all flexural modes present in the 0–1000 Hz bandwidth are excited. The three other actuator sets are implemented as control inputs. Their location was determined in order to allow various control test configurations of interest.

TABLE 2

Center location of actuators

Actuator	z/L	ϕ (degrees)
Disturbance PZT	−0·328	0
Control PZT No. 1	0·370	180
Control PZT No. 2	0·220	60
Control PZT No. 3	−0·395	250

The discrete structural acoustic sensor implemented on the cylinder uses 12 accelerometers (PCB Piezo-electric ICP accelerometers—Model 352A10). The point sensors are arranged as 2 rings of 6 accelerometers equally spaced according to

$$\begin{cases} \phi_{q_1} = q_1 \Delta\phi, & q_1 = 0, 1, \ldots, Q_\phi - 1, \quad \Delta\phi = 2\pi/Q_\phi, \\ z_{q_2} = -L + \Delta z/2 + q_2 \Delta z, & q_2 = 0, 1, \ldots, Q_z - 1, \quad \Delta z = 2L/Q_z, \end{cases} \tag{7}$$

where $Q_z = 2$ and $Q_\phi = 6$ are the number of points along the axial and circumferential direction, respectively. Note that the accelerometers located at $\phi = 0^\circ$ are aligned with the disturbance actuator such as to coincide with an anti-node of the modes excited by the disturbance input. As it will be discussed later, the sensor accuracy is independent of the point sensor circumferential locations when the number of sensors along the circumferential direction is greater than the highest circumferential order of the modes present in the bandwidth. When this condition is not satisfied, however, care must be taken that the point sensors do not coincide with the nodal lines of a given mode (mode $n = 3$ in this case). Furthermore, placing the sensors on anti-nodal lines ensures better signal to noise ratio, thus improving the accuracy of the sensor estimate.

4.2. CONTROL AND MEASUREMENT SET-UPS

For all experimental testing, the cylinder is excited through the disturbance actuator with a band-limited random noise. The sensor accuracy tests are performed over a 200–630 Hz bandwidth while the control tests use a 200–500 Hz bandwidth. The reduced bandwidth associated with the control tests ensures that the 2 by 6 sensor (i.e., 12 accelerometers total) yields relatively accurate estimates over the frequency range. A three channel Filtered-x LMS algorithm [22] is implemented on a Texas Instrument TMS320C30 digital signal processor (DSP) to provide up to three control signals (see Figure 2). The experimental results presented in this paper are limited to cases where only the first and second control actuators were excited (see Table 2). The controller's reference signal is taken from the signal fed to the disturbance actuator. Most of the control tests include an artificial delay of 20 samples in the disturbance path so as to improve system causality. A few cases were also run with a zero delay in order to evaluate the influence of system causality on the control performance. All control tests use the following settings: the sampling frequency is set to $F_S = 2000$ Hz, the FIR compensators have 50 coefficients, and the IIR filters modelling the filtered-x path transfer functions have 60 coefficients in both numerator and denominator. All tests use three error signals based on the structural acoustic sensor and far-field error microphones (B&K 1/2 in microphone, Model 4166), respectively. The sensor's array of filters is implemented on a second TMS320C30 digital DSP. Note that both controller and sensing code could be implemented on a single DSP if desired. Three error microphones are also located along $\theta = 70^\circ$, $\theta = 90^\circ$, and $\theta = 110^\circ$, in the $\phi = 0^\circ$ plane at $R = 1{\cdot}85$ m, while several sets of FIR filters were designed to provide pressure estimates for various radiation angles. All sensor FIR filters have 22 coefficients with a sampling frequency, $F_S = 6000$ Hz. The sensor

transfer functions are accurately modelled up to about 2500 Hz. This wide bandwidth relative to the actual bandwidth of excitation was found necessary in order to ensure stability for the control system. Cases where the response of the sensor filters is not constrained at higher frequencies can lead to unwanted amplification of high frequency content remaining in the system due to the finite roll-offs of the low-pass filters.

All tests were conducted in a 4·2 by 2·2 by 4·5 m anechoic chamber at the Vibration and Acoustics Laboratories (VAL), Virginia Tech. The chamber has an approximate cut-off frequency of 250 Hz. Out-of-plane structural vibrations are measured with a Polytec laser vibrometer (Model OFV-2600/OFV-501). To allow measurements over the entire radiating surface, the laser head is mounted on a one-dimensional linear traverse driven by a stepper motor while a second stepper motor mounted on the end-cap assembly rotates the cylinder around its main axis. The structural velocity measurements used a grid of 13 points along the axial direction and 18 points along the circumferential direction. The measurement point locations are defined by equation (7) with $Q_z = 13$ and $Q_\phi = 18$. This discretization level proved to be sufficient to accurately measure the structural response over the frequency bandwidth of excitation. The sound pressure radiated from the cylinder is measured inside the anechoic chamber with a B&K 1/2 in microphone (Model 4166) mounted on a circular traverse. The traverse microphone is located at a radius of 1·85 m from the center of the cylinder. Due to the legs of the support stand, the traverse can only move in the x–z plane from $\theta = 10^\circ$ to $\theta = 170^\circ$. The rotation of the cylinder also allows measurements along the circumferential direction from $\phi = 0^\circ$ to $\phi = 360^\circ$. All far-field measurements use a grid of $Q_\theta = 13$ points along the azimuthal direction, θ, and $Q_\phi = 18$ points along the circumferential direction, ϕ.

4.3. NUMERICAL SIMULATIONS

In order to study various sensor configurations, numerical simulations were performed prior to the experiments described above. The cylinder structure is modelled under steady-state harmonic excitation of point forces and piezoelectric actuators with a variational approach implementing the Rayleigh–Ritz formulation [15]. In this model, the mechanical displacements and electrical fields within the piezoelectric actuators are fully coupled thus including the mass and stiffness loading of the actuators. This energy based formulation also allows modelling of arbitrary boundary conditions applied along the edges of the cylinder. To this purpose, the model includes translational and rotational springs along the axial, circumferential, and raidal directions. The stiffness factor of each spring can then be adjusted to model arbitrary conditions. The reader is referred to reference [15] for a complete description of the model. The optimal control voltage to each actuator is computed using standard Linear Quadratic Optimal Control theory [2], where the cost function to be minimized is a quadratic function of the control voltage amplitudes.

Table 3 presents the natural frequencies of the first few modes of the cylinder as obtained from the numerical model and experimental modal analysis of the test structure, respectively. Examination of the associated mode shapes reveals that the

TABLE 3

Comparison of the numerical and experimental natural frequencies

Mode (m, n)	Modelled (Hz)	Measured (Hz)
(1, 2)	240·8	241·2
(1, 2)*	241·0	244·2
(1, 3)	304·9	302·9
(1, 3)*	305·5	303·1
(2, 3)	498·8	497·0
(2, 3)*	499·2	500·3
(1, 4)	547·6	540·6
(1, 4)*	547·8	541·1
(1, 1)	565·3	708·0
(1, 1)*	565·5	–
(2, 4)	609·1	601·7
(2, 4)*	609·2	604·6

structure's attachment creates approximately simply-supported boundary conditions where the first modal index, m, is associated with the axial direction, and the second index, n, with the circumferential direction. Note that each mode of vibration is associated with two distinct natural frequencies and mode shapes (i.e., $\cos(n\theta)$ and $\sin(n\theta)$ angular variation) rotated along the circumferential direction by $\pi/(2n)$ relative to one another. This behavior is expected due to the asymmetry introduced by the added mass and stiffness of the piezoelectric actuators. Disregarding the mismatch of mode (1, 1), good agreement between numerical and experimental natural frequencies can be observed. Including the circumferential dependence of the stiffness factors used to model the boundary conditions would possibly improve the match especially for the (1, 1) "beam" mode.

5. SENSOR ACCURACY

This section successively presents analytical and experimental results showing the accuracy of the structural acoustic sensor. The sensor estimate is compared to the actual sound pressure radiated in the far field over the 200–680 Hz bandwidth.

5.1. ANALYTICAL RESULTS

Figure 4 shows the magnitude of the far-field radiated pressure in direction $(\theta, \phi) = (70^\circ, 240^\circ)$ (solid line) along with the sensor estimate based on the piston approximation and two different point sensor configurations. Both results were calculated using the analytical model of the cylinder and its associated radiation field which are described in detail in reference [15]. The "actual" pressure corresponds to the full analytical prediction while the sensor estimate is the far-field pressure estimated using the analytical model in conjunction with the

structural acoustic sensor theory of section 2.2. The dashed line corresponds to a 8 by 7 sensor, i.e., the acceleration measurement points are located according to equation (7) with $Q_z = 8$ and $Q_\phi = 7$, and the dotted line to a 2 by 12 sensor. Recalling the natural frequencies given in Table 3, the resonance peaks correspond, as frequency increases, to modes (1, 2), (1, 3), (2, 3), (1, 4), (1, 1) and (2, 4) where the first and second index referes to the axial and circumferential order, respectively. Note the unusual characteristics of cylinders for which the fundamental mode (1, 1) is not associated with the lowest resonance frequency [18]. As seen on the plot, the 8 by 7 sensor yields excellent accuracy at the resonance frequency of all modes included in the bandwidth except for modes (1, 4) and (2, 4) where large errors can be observed. Considering the 2 by 12 sensor, excellent accuracy is obtained at the resonance frequency of all modes except for a small error near resonance of modes (2, 3) and (2, 4). These results illustrate two fundamental properties of the sensor estimate for cylindrical geometries as outlined below.

Analogous to the case of planar radiators, the far-field radiated pressure in equation (3) can be expressed in terms of the two-dimensional wave-number transform of the structural out-of-plane acceleration [15]. The wave-number transform along the circumferential direction maps a periodic spatial distribution with period 2π into two sets of wave-number components (or Fourier coefficients)

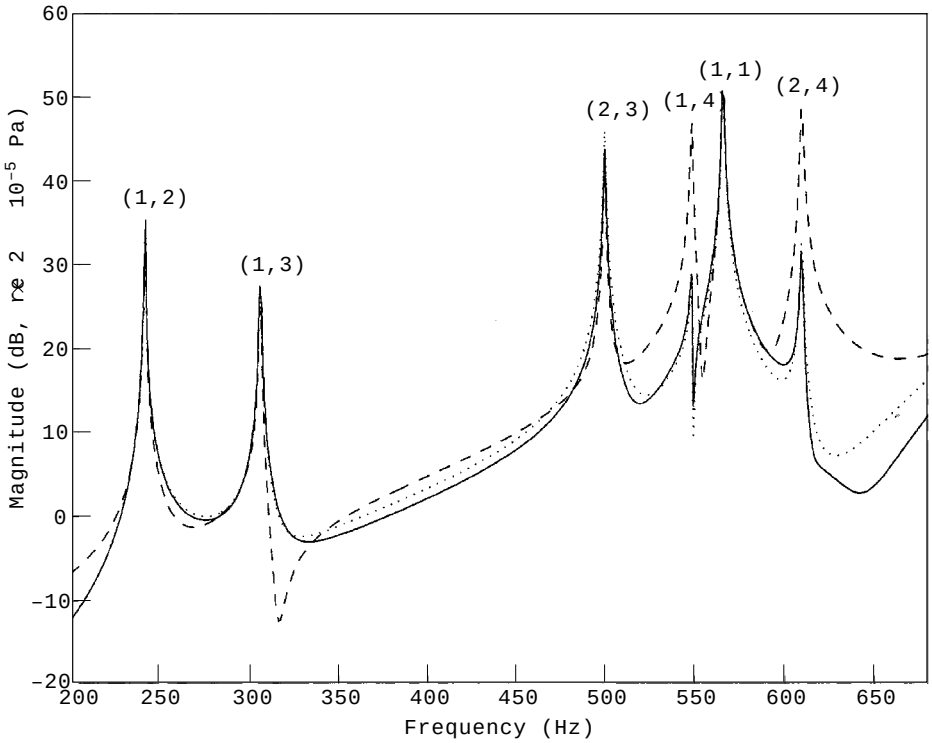

Figure 4. Actual and estimated far-field pressure in direction $(\theta, \phi) = (70^\circ, 240^\circ)$. ——, actual; ----, $Q_z = 8$, $Q_\phi = 7$; · · · · · , $Q_z = 2$, $Q_\phi = 12$.

defined over a discrete set of wave-numbers, $n = 0, 1, \ldots, +\infty$, while the transform along the axial direction maps a finite length axial distribution into a wave-number distribution extending from $-\infty$ to $+\infty$. Now considering a sensor based on the monopole approximation and a set of equally spaced measurement points, the resulting estimate can be expressed in terms of the associated discrete wave-number transforms as [15]

$$p_d(R, \theta, \phi) = -\frac{\rho\, \mathrm{e}^{-jkR}}{\pi kR \sin\theta} \sum_{n=0}^{+\infty} \frac{j^{n+1}}{H_n^{(2)'}(ka \sin\theta)} \{\tilde{\tilde{w}}^{\,c}_{d,n}(k \cos\theta) \cos(n\phi) + \tilde{\tilde{w}}^{\,s}_{d,n}(k \cos\theta) \sin(n\phi)\}, \tag{8}$$

where

$$\tilde{\tilde{w}}^{\,c}_{d,n}(\gamma) = \frac{\Delta\phi}{\pi\varepsilon_n} \sum_{q_1=0}^{Q_\phi - 1} \tilde{\tilde{w}}_d(\phi_{q_1}, \gamma) \cos(n\phi_{q_1})$$

$$\tilde{\tilde{w}}^{\,s}_{d,n}(\gamma) = \frac{\Delta\phi}{\pi\varepsilon_n} \sum_{q_1=0}^{Q_\phi - 1} \tilde{\tilde{w}}_d(\phi_{q_1}, \gamma) \sin(n\phi_{q_1})$$

$$\text{and} \quad \tilde{\tilde{w}}_d(\phi, \gamma) = \Delta z \sum_{q_2=0}^{Q_z - 1} \ddot{w}(\phi, z_{q_2})\, \mathrm{e}^{j\gamma z_{q_2}}. \tag{9}$$

Note that the actual radiated pressure is obtained by replacing $\tilde{\tilde{w}}^{\,c}_{d,n}(\gamma)$ and $\tilde{\tilde{w}}^{\,s}_{d,n}(\gamma)$ in equation (8) by their continuous equivalent

$$\tilde{\tilde{w}}^{\,c}_{n}(\gamma) = \frac{1}{\varepsilon_n \pi} \int_{-\infty}^{+\infty} \int_0^{2\pi} \ddot{w}(\phi, z) \cos(n\phi)\, \mathrm{e}^{j\gamma z}\, \mathrm{d}\phi\, \mathrm{d}z,$$
$$\tilde{\tilde{w}}^{\,s}_{n}(\gamma) = \frac{1}{\varepsilon_n \pi} \int_{-\infty}^{+\infty} \int_0^{2\pi} \ddot{w}(\phi, z) \sin(n\phi)\, \mathrm{e}^{j\gamma z}\, \mathrm{d}\phi\, \mathrm{d}z. \tag{10}$$

The pressure radiated in the far field at a particular angle is associated with a single axial wave-number component, $k \cos(\theta)$, within the supersonic region, $[-k, +k]$, and an infinite number of circumferential wave-numbers, $n = 0, 1, \ldots, +\infty$. In practice, the infinite summation can be truncated based on the highest order of the circumferential modes included in the response and the range of the non-dimensional parameter, ka, as the magnitude of the Hankel derivative tends towards infinity as n increases.

From equation (9), the accuracy of the sensor estimate is dictated by the levels of aliasing occurring in the axial and circumferential discrete wave-number transforms. The number of point measurements along the axial direction, Q_z, should be such that the Nyquist axial wave-number, $K_S/2 = Q_z\pi/(2L)$, remains above the main axial wave-number components of the acceleration distribution. Likewise, the circumferential Nyquist wave-number, $K_S/2 = Q_\phi/2$, should be greater than the highest circumferential order of the modes found in the structural response. This requirement is a direct consequence of the sampling theorem commonly applied to the sampling of time domain signals. It should be pointed out that unlike the axial wave-number transform which extends up to infinity

regardless of the spatial distribution due to the finite cylinder length, the circumferential wave-number transform only contains the components associated with modes found in the distribution. Therefore, while the axial discrete wave-number transform always results in some level of aliasing, the discrete circumferential wave-number transform will yield no aliasing, i.e., perfect estimates, provided all components above the Nyquist wave-number have zero amplitude. In addition, all or part of the wave-number components associated with circumferential wave-numbers above the Nyquist wave-number will yield large errors due to the periodicity of the discrete wave-number transform. Thus, the Nyquist circumferential wave-number should be high enough such that errors associated with higher wave-numbers are cancelled by the large magnitude of the Hankel derivative term. Finally, it can be shown that the circumferential wave-number component estimate is independent of the origin of the point sensors locations along ϕ provided the number of measurement points satisfies the sampling theorem along this direction. Note that similar trends are expected for the piston approximation.

Returning to Figure 4, the axial wave-number transform on resonance features a main peak around $\gamma = m\pi/(2L)$ where m is the axial modal index. Consequently, the number of measurement points along the axial direction should be greater than the modal index of the mode dominating the response, i.e., $Q_z > m$. Similarly, the number of point measurements along the circumferential direction should be greater than twice the modal index of the associated mode, i.e., $Q_\phi > 2n$. Cases where at least one of the above conditions is not satisfied yield aliasing errors as shown in Figure 4. At off-resonance frequencies, the response includes higher order modes which reduce the accuracy of the estimate. Note that the discretization level is the critical parameter affecting the sensor estimate. In other words, good sensor accuracy is ensured over the entire radiating field as long as the number of measurement points is high enough relative to the dominant modes of the response. Finally, it should be mentioned that the above results assume perfect modelling of the sensor transfer functions. However, due to the relative simple characteristics of the sensor transfer functions, excellent modelling accuracy can be achieved with only a few FIR coefficients [15]. Other analytical results, not presented here for brevity, also confirm that Discrete Structural Acoustic Sensing will provide good estimates of radiated pressure as long as no significant aliasing occurs.

5.2. EXPERIMENTAL RESULTS

This section briefly presents the accuracy of the 2 by 6 sensor which is implemented experimentally on the cylinder. The cylinder is excited through the disturbance piezoelectric actuator with a band-limited random noise over 200–630 Hz. As true far-field conditions do not exist in the anechoic chamber especially at low frequencies due to its limited size relative to the dimensions of the cylinder and the acoustic wave-length within the frequency bandwidth of excitation, the pressure radiated in the far field is ''reconstructed'' from the laser measurements of the cylinder out-of-plane velocity. Analogous to the real time pressure estimate implemented in the sensor, the pressure field is computed off-line

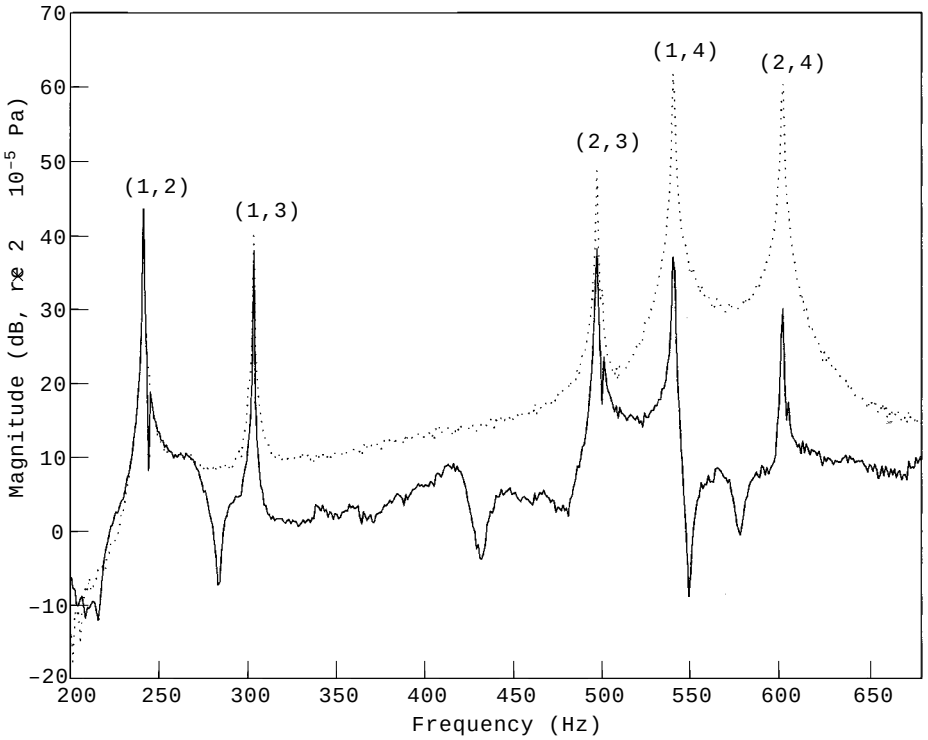

Figure 5. Reconstructed and estimated far-field pressure in direction $(\theta, \phi) = (76{\cdot}8^\circ, 0^\circ)$. ——, reconstructed pressure; · · · · ·, sensor output.

from the structural laser measurements and the associated Green's function replacing the continuous integral in equation (3) by its discrete approximation [15]. However, in this case, the discretization level is much higher with a grid of 13 by 18 measurement points (see section 4.2) thus ensuring a high fidelity in the predicted far-field sound pressure. The magnitude of the reconstructed pressure at an angle $(\theta, \phi) = (76{\cdot}8^\circ, 0^\circ)$ is compared to the associate sensor estimate in Figure 5. Recalling the system's natural frequencies presented in Table 3, five flexural modes have their natural frequencies within the 200–630 Hz bandwidth. With increasing frequency, the five main resonance peaks noticed on the plot correspond to modes (1, 2), (1, 3), (2, 3), (1, 4), and (2, 4), respectively. Notice that the response also exhibits small contribution from "double" modes (1, 2)*, (2, 3)*, and (2, 4)*.

Examining the sensor output (dotted line), the pressure estimate shows good accuracy around the resonance frequency of the (1, 2) mode. A small variation of about 2 dB is observed at the resonance frequency of mode (1, 3). The reconstructed pressure is also relatively well estimated at off-resonance frequencies around the (1, 2) mode. The sensor accuracy then deteriorates as the frequency increases. A 6 dB variation between reconstructed and estimated pressure is noticed at the resonance frequency of mode (2, 3) while the estimated pressure at the resonance frequencies of the last two modes in the bandwidth (modes (1, 4) and (2, 4)) is off by more than 20 dB.

The above tendencies confirm the analytical results discussed in the previous section and agree well with the properties of the sensor estimate. As mentioned earlier, $Q_z = 2$ measurement points along the axial direction yield good estimates for modes of axial order 1 or less. In the circumferential direction, $Q_\phi = 6$ measurement points ensure accurate estimates of modes up to $n = 2$. That is to say, spatial distributions that are dominated by modes with axial and circumferential order larger than one and two, respectively, do not yield accurate pressure estimates. Increasing the number of point structural sensors would in turn increase the accuracy of the sensor prediction for these higher order modes.

6. RADIATION CONTROL

The following two sections discuss the analytical and experimental control results. In both cases, the cylinder is under broadband excitation through the disturbance actuator. In order to evaluate the performance of the structural acoustic sensor, results are presented which compare its control performances to those obtained with error microphones located in the far field. Note that the following analysis focuses on the influence of the "error" information on the control performances. In particular, the system is not optimized in terms of control input and/or error measurement locations to achieve the best possible attenuation in radiated power over the frequency bandwidth of excitation.

6.1. ANALYTICAL RESULTS

This section presents three control cases calculated using the analytical model. The first two cases are based on the minimization of the estimated and actual radiated pressure in directions $(\theta, \phi) = (70^\circ, 0^\circ)$, $(110^\circ, 40^\circ)$, $(90^\circ, 160^\circ)$, $(70^\circ, 240^\circ)$, and $(110^\circ, 320^\circ)$. These five radiation angles were chosen such as to obtain good global sound attenuation, i.e., none of the modes included in the frequency bandwidth have radiation nodal lines along all five angles. A third control case involves the direct minimization of the out-of-plane acceleration measured at the point structural sensor locations corresponding to the Active Vibration Control case for this system. Note that for the AVC case, the number of error signals then equals the number of accelerometers implemented in the sensor, i.e., 12, while the ASAC cases use five error signals corresponding to the directions of pressure estimates. All three cases use the same control input configuration: the actuators' locations are those given in Table 2 except for the circumferential angle of the third control actuator which was set to $\phi = 225^\circ$. All three control actuators are implemented as control inputs in the following results. Note that this configuration yields an over-determined system such that the optimal control amplitudes are solved in the least square sense. The cost function thus does not include the control effort usually required to condition the solution of under-determined systems [22].

Figure 6 shows the calculated radiated sound power before control (solid line) and after control based on the three cost functions. The dashed line corresponds to the minimization of the five pressure estimates using a 3 by 9 structural acoustic sensor ($Q_z = 3, Q_\phi = 9$), the dotted line corresponds to the minimization of the

actual radiated pressure in the same directions, and the dashed-dotted line corresponds to the minimization of the out-of-plane acceleration at the point sensor locations (see equation (7)). The sound power is computed by integrating the closed form solution of the far-field pressure over the sphere surrounding the cylinder. The reader is referred to reference [15] for a complete derivation.

As seen on the controlled response, the first two sensing approaches (dashed and dotted lines) yield very close control performances. The radiated sound power is attenuated over the entire bandwidth with very small control spillover. The total attenuation across the bandwidth is 20·2 dB for the structural acoustic sensor and 19·4 dB for the error microphones. These results are expected since the discretization level of the sensor ensures reduced aliasing errors for acceleration distributions including modes with axial and circumferential order up to 2 and 4, respectively. In other words, all modes included in the bandwidth yield accurate pressure estimates. Note that minimizing the actual radiated pressure yields a slight decrease in overall sound attenuation thus suggesting the small errors introduced in the pressure estimates result in a slightly more global error information for this particular set of minimization angles. These results show that the structural acoustic sensor implemented in this case can effectively replace the

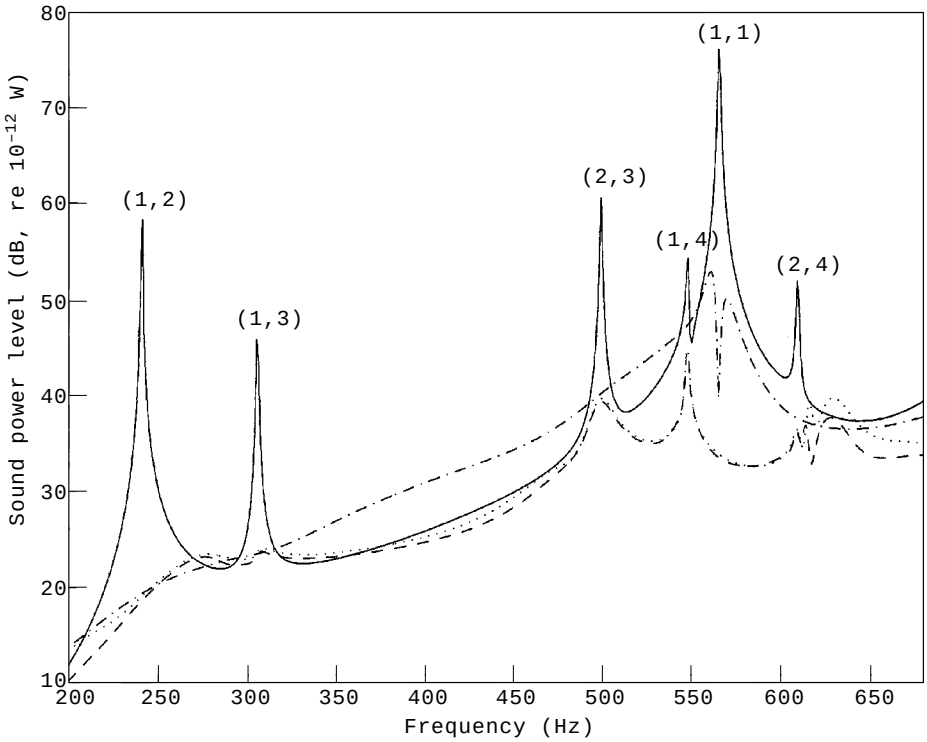

Figure 6. Calculated radiated sound power—minimization of pressure estimate in directions $(\theta, \phi) = (70^\circ, 0^\circ), (110^\circ, 40^\circ), (90^\circ, 160^\circ), (70^\circ, 240^\circ)$, and $(110^\circ, 320^\circ)$. ——, before control; ----, after control, 3 by 9; · · · · ·, after control, microphones; –·–·, after control, acceleration.

TABLE 4

Calculated total attenuation levels over the frequency bandwidth of excitation

Control case	Attenuation (dB)	
	Mean-square velocity	Sound radiated power
3 by 9 structural acoustic sensor	8·1	20·2
Error microphones	8·3	19·4
3 by 9 accelerometer array	20·7	12·4

error microphones. Comparatively, a reduced number of acceleration measurement points would increase aliasing errors in the sensor estimate and in turn reduce the global sound attenuation levels. Note that the predicted control performance near resonance of mode (1, 1) may be inaccurate. As mentioned earlier, the analytical model does not estimate correctly the resonance frequency of this mode (see Table 3) and control results near its resonance should therefore be interpreted carefully.

The third cost function associated with the minimization of the discrete acceleration over 27 points (dashed-dotted line) does not perform as well as the two previous cost functions based on radiation information. While similar levels of attenuation are achieved at on-resonance frequencies (except near resonance of the (1, 1) mode), the control performance significantly deteriorates at off-resonance frequencies. This behavior suggests that some level of modal restructuring occurs off-resonance when minimizing radiation information. In this case, the controller achieves attenuation in the far field by combining several structural modes that are present in the uncontrolled response. The overall vibration levels do not necessarily decrease in this case. At on-resonance frequencies, a single mode dominates the structural response and radiation control is then achieved through modal reduction. To further illustrate these results, the overall attenuation levels of mean-square velocity and sound radiated power are presented in Table 4 for the three cost functions. Again, the first two cost functions based on radiation information perform almost identically. The third cost function based on structural information increases the overall attenuation level in mean-square velocity by more than 10 dB. However, the attenuation in sound radiated power decreases by about 8 dB. In other words, minimizing the structural vibrations yields, in this case, decreased control performances in terms of radiated sound attenuation when compared to the use of structural acoustic sensoring or error microphones.

It should be mentioned that the above results are based on an optimal control solution in the frequency domain which presents a number of limitations when used to predict the performance of a real time domain control system under broadband frequency disturbances. Specifically, the optimal control transfer functions are not constrained to yield realizable FIR filters. This often leads to over-estimating the controller performance and, in some cases, to control spillover not observed experimentally due to the finite number of coefficients in the control

compensator among other factors. Consequently, the analytical results presented above do not accurately model the performance of the control system investigated experimentally. However, they still provide insight into the control performance of Discrete Structural Acoustic Sensing compared to other sensing approaches and also indicate the maximum achievable performance.

6.2. EXPERIMENTAL RESULTS

This section discusses some of the control results obtained experimentally on the system described previously. The first two cases use the 2 by 6 structural acoustic sensor to provide error signals associated with pressure estimates in three directions. A third case uses three error microphones located along the same directions for comparison purpose. All three cases use the first two control actuators, leaving the third actuator unexcited. The radiated sound power presented below is estimated from the multiple traverse microphone measurements over the sphere surrounding the cylinder.

The first control case corresponds to the minimization of the three sensor outputs associated with pressure estimates in directions $(\theta, \phi) = (76{\cdot}8^\circ, 340^\circ)$, $(63{\cdot}5^\circ, 0^\circ)$, and $(103{\cdot}2^\circ, 0^\circ)$, respectively. Figure 7 shows the radiated sound power before and after control. The dashed line corresponds to the standard configuration where a 20-sample delay is included in the disturbance path. The

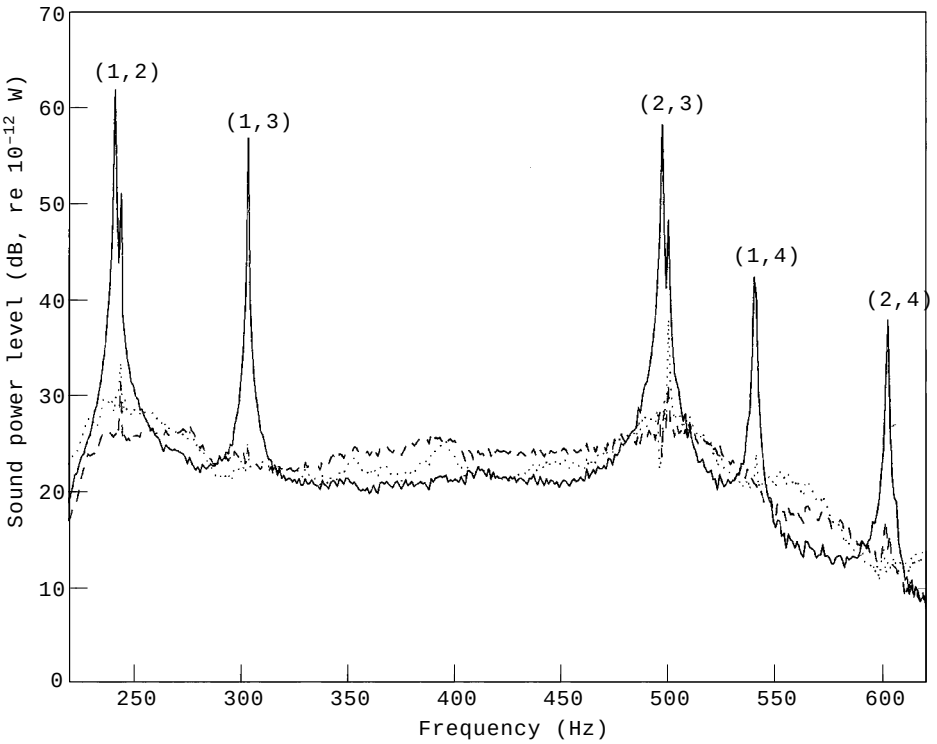

Figure 7. Measured radiated sound power—minimization of pressure estimates in directions $(\theta, \phi) = (76{\cdot}8^\circ, 340^\circ)$, $(63{\cdot}5^\circ, 0^\circ)$ and $(103{\cdot}2^\circ, 0^\circ)$: ——, before control; ----, after control (20-sample delay); · · · · ·, after control (no delay).

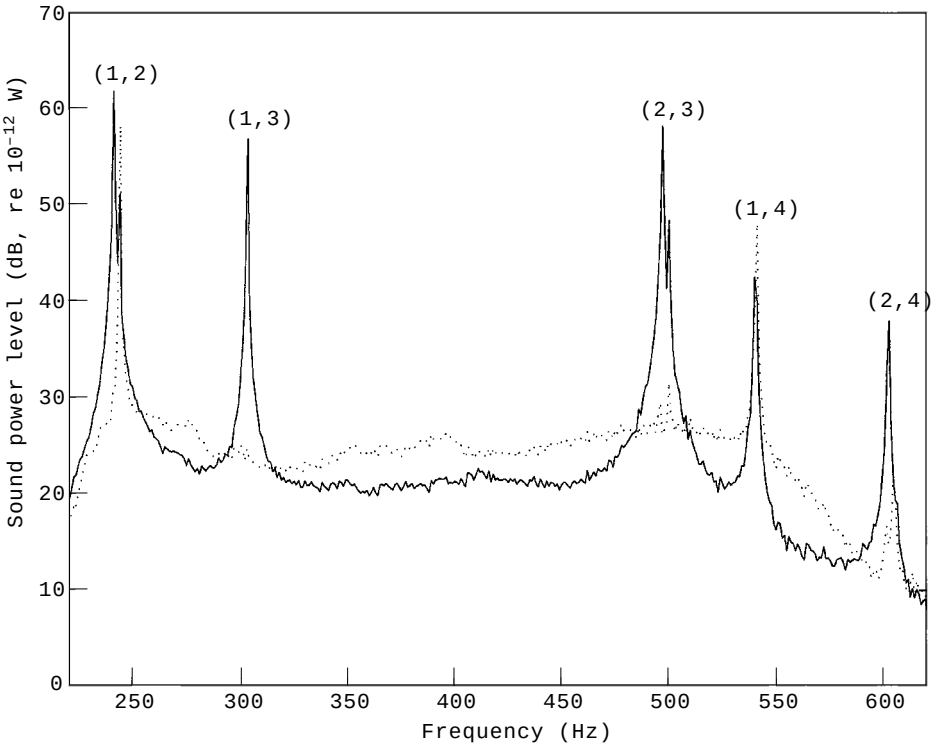

Figure 8. Measured radiated sound power—minimization of pressure estimates in directions $(\theta, \phi) = (70^\circ, 0^\circ)$, $(90^\circ, 0^\circ)$, and $(110^\circ, 0^\circ)$: ——, before control; · · · · ·, after control.

dotted line corresponds to an additional case based on the same control and error configuration with no delay included in the disturbance path. In both cases, the radiated sound power is attenuated by 20 dB or more near all resonance frequencies of the uncontrolled response. Small increases in sound power can be observed at off-resonance frequencies for both cases. Note that the dotted line associated with a possible acausal system does not show significant loss in performance compared to the dashed line. In other words, system causality does not appear to be a critical factor in this case. Due to the small levels of damping present in the system, the response is largely dominated by the five resonance frequencies of the modes included in the bandwidth. It is therefore highly predictable allowing control regardless of the system's causality. The total reduction level in radiated sound power achieved across the frequency bandwidth of excitation is 15·4 dB with the 20-sample delay and 15·0 dB with no delay. Note that the three directions of minimization ensure good global control, i.e., no spillover is observed on the radiated sound power of the controlled response. In other words, the controller is forced to attenuate the amplitude of all modes in order to minimize all three error signals. Modal reduction is therefore the main control mechanism involved in this case.

The second control case based on the structural acoustic sensor uses three pressure estimates in directions $(70^\circ, 0^\circ)$, $(90^\circ, 0^\circ)$, and $(110^\circ, 0^\circ)$. These three directions of minimization correspond to the locations of the error microphones

implemented in the next control case. Figure 8 shows the radiated sound power before and after control. Excellent attenuation levels can be observed near resonance of modes (1, 2), (1, 3), (2, 3) and (2, 4) while significant control spillover is noticed near resonance of modes (1, 2)* and (1, 4)*. The total attenuation in radiated sound power is 5·9 dB. In this case, all directions of minimization are in the $\phi = 0^\circ$ plane which coincides with radiation nodal line of modes (1, 2)*, (1, 4)* and (2, 4)*. In other words these modes are not well observed by the three error signals. This explains the increase in radiated sound power noticed near resonance of modes (1, 2)* and (1, 4)*: rather than cancelling the associated modal amplitudes, the controller recombines the modal amplitudes of the "double" modes and rotates the acceleration distribution such that the resulting nodal lines are aligned with the minimization angles. This modal restructuring mechanism is illustrated in Figure 9 where the out-of-plane velocity distribution measured by the laser vibrometer is shown before and after control at 541 Hz, i.e., near resonance of mode (1, 4). The acceleration distribution after control is clearly rotated. Note that modal restructuring does not occur near resonance of modes (1, 3) and (2, 3). The first two control actuators are aligned with the anti-nodal

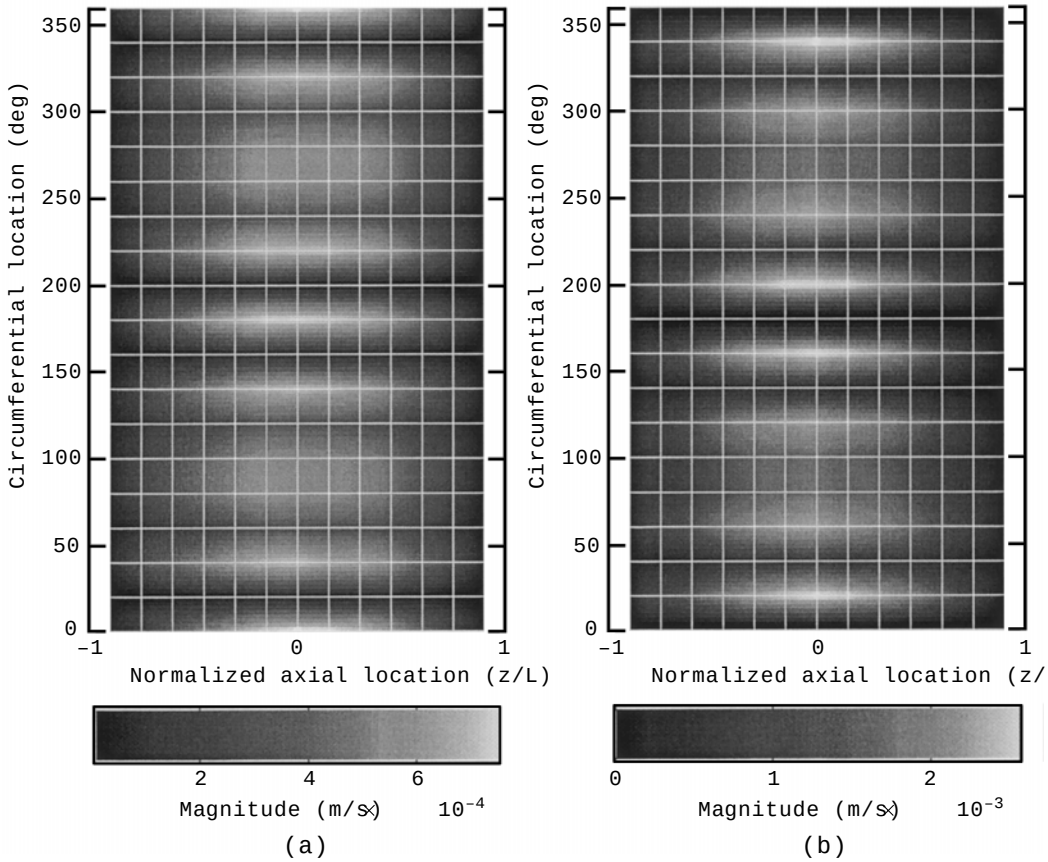

Figure 9. Measured out-of-plane velocity distribution at 541 Hz; minimization of pressure estimates in directions $(\theta, \phi) = (70^\circ, 0^\circ)$, $(90^\circ, 0^\circ)$ and $(10^\circ, 0^\circ)$: (a) before control, (b) after control.

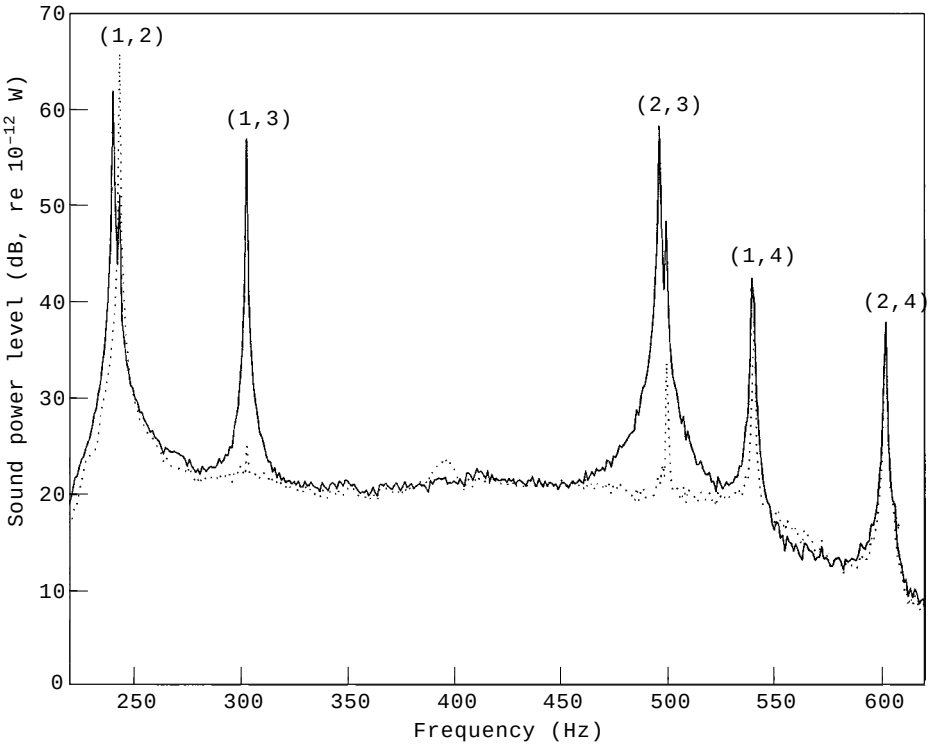

Figure 10. Measured radiated sound power—minimization of pressure at error microphones in directions $(\theta, \phi) = (70^\circ, 0^\circ)$, $(90^\circ, 0^\circ)$, $(110^\circ, 0^\circ)$: ——, before control; · · · · · , after control.

lines of the associated "double" modes (1, 3)* and (2, 3)*, therefore preventing their excitation. It should be pointed out that the previous case does not allow the above modal restructuring as the error signals do not correspond to pressure estimates along circumferential angles multiple of 45°, i.e., one error signal at least observes the "double" modes thereby forcing the controller to reduce the associated vibrations. These results therefore confirm the relatively good accuracy of the structural acoustic sensor implemented on the cylinder. Despite the small level of discretization ($Q_z = 2$, $Q_\phi = 6$) which only provides accurate estimates near resonance of mode (1, 2), the sensor still yields error information somewhat related to the radiated sound pressure at higher frequencies. This is further illustrated by comparing these results with the next control case based on far-field error microphones.

The third control case replaces the outputs of the structural acoustic sensor by three error microphones located in the far field. To facilitate the comparison of the two sensing approaches, this case uses the same control configuration as previously. In particular, the three error microphones are located along the same directions of pressure estimates implemented in the previous case. The radiated sound power estimated from the traverse microphone measurements is presented before and after control in Figure 10. As for the case of pressure estimates using Discrete Structural Sensing (see Figure 8), excellent global sound attenuation is achieved near resonance of modes (1, 2), (1, 3) and (2, 3). Modal reduction occurs

at these frequencies, therefore cancelling the sound pressure radiated over the entire field. Similarly, the sound power near resonance of mode (1, 2)* increases as in the previous control case based on the structural acoustic sensor. Again, this mode has a radiation nodal line along $\phi = 0^\circ$ and thus remains unobserved by any of the three error microphones. Note that the control spillover at this frequency is larger than in the previous control case. As a result, the total sound radiated power across the frequency bandwidth of excitation increases by 0·7 dB. Similar behavior can be observed near resonance of modes (1, 4)* and (2, 4)*. This case clearly illustrates the importance of the control actuator and error sensor configurations. In particular, global sound attenuation for lightly damped cylindrical radiators can only be achieved through modal reduction. As a final remark, it should be mentioned that the controlled response based on pressure estimates in the same three directions and the same two control actuators exhibits very similar trends as the ones obtained with error microphones. In particular, the structural acoustic sensor yields nearly the same response near resonance of modes (1, 2) and (1, 2)* which confirms the accuracy of the pressure estimates at these frequencies. Also, note that the structural acoustic sensor yields better performance in terms of radiated sound power attenuation near resonance of mode (2, 4) compared to the error microphones. This behavior suggests that both (2, 4) and (2, 4)* modes are observed by the structural acoustic sensor due to errors in the pressure estimates. Consequently, unlike the error microphones, the structural acoustic sensor prevents modal restructuring, thus increasing global sound attenuation.

7. CONCLUSIONS

Broadband radiation control from a finite cylinder has been demonstrated both analytically and experimentally. The ASAC system implements a multi-channel Filtered-x LMS control algorithm. Structural control inputs are applied through piezoelectric actuators while error information is provided by a discrete structural acoustic sensor. Results show attenuation in total radiated sound power of up to 15 dB is achieved across a frequency bandwidth encompassing the first five flexural modes of the cylinder.

These results also validate the extension of Discrete Structural Acoustic Sensing to baffled cylindrical geometries. In this technique, the sensor constructs real time estimates of the presure radiated in the far field at prescribed angles from discrete structural acceleration measurements and associated signal processing. Sensor accuracy and comparisons of control performances based on Discrete Structural Acoustic Sensing and the use of far-field error microphones, respectively, demonstrate the ability of the structural acoustic sensor to replace direct far-field pressure measurements. In particular, the analytical results show the minimizing a cost function based on sensor estimates yields similar control performance to that obtained with a cost function based on actual far-field pressure, provided accuracy is ensured for the sensor. The experimental results on broadband radiation control confirm this results. Similar control performances are obtained for both types of error information. Examination of the system's response at single

frequencies within the bandwidth of excitation also reveals the controller behaves similarly in each case. This includes frequencies where modal restructuring is the main control mechanism which confirms the ability of the sensor to provide accurate radiation information.

The accuracy of the sensor estimate over a given frequency bandwidth is primarily related to the number of structural measurements implemented in the sensor. In particular, for equally spaced measurements points, accuracy of the sensor estimates is ensured provided the following two conditions are satisfied. First, the number of measurement points along the cylinder main axis should be such that the associated Nyquist wave-number (half the spatial sampling frequency) is located on the wave-number axis above the main content of the wave-number transform of the structural out-of-plane motion along this axis. In terms of simply-supported mode shapes, this first requirement is satisfied if the number of measurement points along the main axis is greater than the highest order along the same axis of the modes which dominate the response. Second, the number of measurement points along the circumferential direction of the cylinder should be greater than twice the order of the highest circumferential order of the modes dominating the response. These conditions define the frequency bandwidth of accuracy for the structural acoustic sensor.

More generally, the design and implementation of the sensor do not require precise knowledge of the vibration characteristics of the structure. While some knowledge of the structural velocity distributions allows for predicting the accuracy of the pressure estimate and pre-determining the appropriate discretization level, the sensor transfer functions strictly depend on the geometry of the structure and the surrounding fluid properties. This differs from a number of alternative structural sensing techniques whose design and implementation are directly based on dynamic properties of the structure, such as mode shapes. In comparison, Discrete Structural Acoustic Sensing provides a more robust error information. The modelling of the sensor transfer functions involves simple Finite Impulse Response (FIR) filters. This type of filter is well suited to represent the radiation of monopole and piston sources into an unbounded medium. In particular, the sensor transfer functions do not feature resonances, which would otherwise require the use of the more complex Infinite Impulse Response (IIR) filter model. Finally, when implemented in a far-field radiation control system, the time delay associated with the acoustic path can be removed from the sensor transfer functions without affecting the controller performance. This property greatly simplifies the sensor digital filters by reducing the number of coefficients required for accurate modelling of the sensor transfer functions. The sensor DSP implementation then becomes very efficient in terms of computations, allowing higher sampling frequencies or the combination of the sensor and controller code on a single DSP.

ACKNOWLEDGMENTS

The authors gratefully acknowledge support by the Office of Naval Research, Dr Kam Ng, Technical Monitor. The authors also wish to thank Kent Schuster

and Scott Kelly at Reynold's Metal Company in the Extrusion Division for donating the aluminum cylinder used in the experiments.

REFERENCES

1. C. R. Fuller 1990 *Journal of Sound and Vibration* **136**, 1–15. Active control of sound transmission/radiation from elastic plates by vibration inputs. I. Analysis.
2. C. R. Fuller, S. J. Elliott and P. A. Nelson 1996 *Active Control of Vibration*. London: Academic Press.
3. E. F. Crawley and J. De Luis 1987 *AIAA Journal* **25**, 1373–1385. Use of piezoelectric actuators as elements of intelligent structures.
4. C. R. Fuller, C. H. Hansen and S. D. Snyder 1989 in *Proceedings of Inter-Noise* 89, 509–511. Active control of structurally radiated noise using a piezoceramic actuator.
5. R. L. Clark and C. R. Fuller 1992 *Journal of the Acoustical Society of America* **91**, 3313–3320. Experiments on active control of structurally radiated sound using multiple piezoelectric actuators.
6. C. R. Fuller and R. A. Burdisso 1991 *Journal of Sound and Vibration* **148**, 335–360. A wavenumber domain approach to active control of structure-borne sound.
7. C. K. Lee and F. C. Moon 1990 *Journal of Applied Mechanics* (*Transactions of the ASME*) **57**, 434–441. Modal sensors/actuators.
8. Yi Gu, R. L. Clark, C. R. Fuller and A. C. Zander 1994 *ASME Journal of Vibration and Acoustics* **116**, 303–308. Experiments on active control of plate vibration using piezoelectric actuators and polyvinylidene (PVDF) modal sensors.
9. S. D. Snyder, C. H. Hansen and N. Tanaka 1993 in *Proceedings of the Second Conference on the Recent Advances in Active Control of Sound and Vibration* 177-188. Shaped vibration sensors for feedforward control of structural radiation.
10. C. Guigou, F. Charette and A. Berry 1994 in *Proceedings of the Third International Congress on Air- and Structure-Borne Sound and Vibration* 1507–1514. Active control of sound by minimization of volume velocity on finite beam.
11. M. E. Johnson and S. J. Elliott 1993 in *Proceedings of the Institute of Acoustics*, Volume 15, 411–420. Volume velocity sensors for active control.
12. J. P. Maillard and C. R. Fuller 1994 *Journal of the Acoustical Society of America* **95**, 3252–3261. Advanced time domain wave-number sensing for structural acoustic systems. I. Theory and design.
13. J. P. Maillard and C. R. Fuller 1994 *Journal of the Acoustical Society of America* **95**(6), 3262–3272. Advanced time domain wave-number sensing for structural acoustic systems. II. Active radiation control of a simply-supported beam.
14. J. P. Maillard and C. R. Fuller 1995 *Journal of the Acoustical Society of America* **98**, 2613–2621. Advanced time domain wave-number sensing for structural acoustic systems. III. Experiments on active broadband radiation control of a simply-supported plate.
15. J. P. Maillard 1997 *PhD thesis*, *Virginia Polytechnic Institute & State University*. Advanced time domain sensing for active structural acoustic control.
16. C. E. Ruckman and C. R. Fuller 1995 *Journal of Sound and Vibrations* **186**, 395–406. Optimizing actuator locations in active noise control systems using subset selection.
17. R. L. Clark and C. R. Fuller 1994 *Journal of Intelligent Materials Systems and Structures* **5**, 379–391. Active control of structurally radiated sound from an enclosed finite cylinder.
18. M. C. Junger and D. Feit 1986 *Sound*, *Structures and their Interaction*. Boston, MA: MIT Press.
19. M. Abramowitz and I. A. Stegun 1964 *Handbook of Mathematical Functions*. Washington, DC: National Bureau of Standards; see chapter 9.

20. C. A. Brebbia and J. Dominguez 1989 *Boundary Elements—An Introductory Course*. New York: McGraw-Hill.
21. Piezo Systems, Inc. *Product Catalog*. 186 Massachusetts Avenue, Cambridge, MA 02139.
22. P. A. Nelson and S. J. Elliott 1992 *Active Control of Sound*. London: Academic Press.